Fermilab Library
0 1160 0022187 1
DFUB-9-94

DFUB 9/94

HADRON-HADRON ELASTIC SCATTERING AND TOTAL CROSS-SECTIONS AT HIGH ENERGIES

GIORGIO GIACOMELLI
Dipartimento di Fisica dell'Università di Bologna
I.N.F.N., Sezione di Bologna

Invited paper for the 1994 Marshak Memorial Volume

ABSTRACT

A short review is made of the present situation of high energy hadron-hadron elastic scattering and total cross sections at very high energies.

1. Introduction

In this review, the main features of total cross sections and elastic scattering of high energy hadrons will be discussed. The emphasis will be on $\bar{p}p$ collisions at the highest energies. But there will also be a brief discussion of data at lower energies.

Measurements of the "stable" charged hadrons ($\pi^{\pm}, K^{\pm}, p^{\pm}$) were performed on hydrogen and deuteron targets in order to extract the cross sections in pure isospin states: $I = 1/2,\ 3/2$ in πN, $I = 0,\ 1$ in KN, pN, and $\bar{p}N$ interactions. Note that π^+p, K^+p and pp are pure isospin states with $I = 3/2,\ 1,\ 1$, respectively; π^-p K^-p and $\bar{p}p$ are instead mixed states. As the energy increases the difference between the two pure isospin state cross sections tends to zero.

Total cross sections depend on one kinematic variable, the energy, and on the type of colliding particles. In terms of energy one may consider two regions:

i) The low energy region, for $p_{lab} < 5\ GeV/c$, which is characterized by the presence of peaks and other structures. The main purpose of the precise measurements, performed mainly at the Brookhaven AGS in the 1960's, was the search for resonances and structures [1-4].

ii) In the high energy region (for $p_{lab} > 10\ GeV$) the cross sections vary smoothly and slowly with energy. All cross sections, first decrease with increasing energy (with the exception of K^+p), reach a minimum and then increase with energy. The differences $[\sigma_{tot}(\bar{x}p) - \sigma_{tot}(xp)]$ (where $\bar{x}, x$ are π^-, π^+; K^-, K^+; $\bar{p}, p$) decrease and tend towards zero. This is a manifestation of one of the high energy theorems (the Pomeranchuck theorem)[4]. In the very high energy region, where all cross sections increase logarithmically with energy, one is interested in the determination of the high energy parameters σ_{tot}, b, ρ, σ_{el}/σ_{tot}. This last region is the main concern of this paper.

The angular distribution for elastic scattering at low energies has a contribution from coulomb scattering at small angles; at larger angles the angular distribution is due to nuclear scattering and it arises from a number of partial waves, one of which may become dominant when it resonates; the number of partial waves increases as the energy increases.

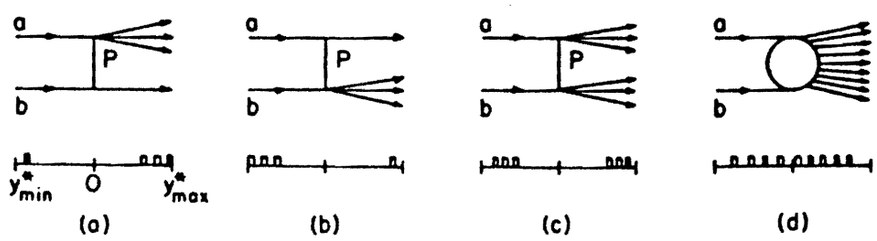

Figure 1 - Pictorial descriptions of production processes with characteristic rapidity distributions. P indicates Pomeron exchange, that is the exchange of the highest Regge trajectory with the quantum numbers of the vacuum. (a) Fragmentation of the beam particle, a. (b) Fragmentation of the target, b. (c) Double fragmentation of a and b. (d) central collision production reaction.

In the very high energy region the differential cross section for the elastic scattering of unpolarized particles from unpolarized targets acquires a new simplicity and depends on two variables: the energy and an angular variable, which is usually chosen to be the square of the four momentum transfer t. The energy dependence is a weak one, of the $ln\ s$ type. The angular distribution may be divided in four regions:

i) The coulomb region for $|t| < 0.001\ (GeV/c)^2$;
ii) The coulomb-nuclear interference region for $0.001 < |t| < 0.01\ (GeV/c)^2$. Measurements in this region yield information on the ratio ρ of the real to the imaginary part of the forward scattering amplitude.
iii) The nuclear diffraction region proper for $0.01 < |t| < 0.5\ (GeV/c)^2$. Here the most important parameter is the slope B, or the slopes b_i, of the diffraction pattern.
iv) The large angle region for $|t| > 0.5\ (GeV/c)^2$. For c.m. energies smaller than 100 GeV, it is characterized by a dip-bump structure which resembles that from diffraction from an opaque disc (but it has some differences).

The experimental results from Serpukhov [5,6], cosmic rays [7], the ISR [8-13], Fermilab [14-15], $S\bar{p}pS$ [15-17] and Fermilab [18-21] brought several changes in the phenomenological picture of high energy hadron-hadron collisions.

In particular, the total cross section measurements performed at Serpukhov in 1969-1971 showed first that some cross sections were not decreasing with energy as fast as expected [5] and then that the K^+p total cross section was increasing with energy [6]. In 1972 there were indications from cosmic ray experiments that also the pN cross section was increasing with energy[7]. In 1973, measurements at the CERN-ISR showed that the pp cross section was rising with energy [10-11]. The measurements of the total cross sections of all charged hadrons on protons and neutrons at Fermilab in 1974-1979 showed that all cross sections were rising with energy [14-15]. The confirmation for the $\bar{p}p$ cross section came later at the $S\bar{p}pS$ and Tevatron colliders[16-21].

The total cross section due to nuclear $p\bar{p}$ scattering arises from a number of processes, which may be classified for our purposes as follows (Fig. 1):

$$\sigma_{tot} = \sigma_{el} + \sigma_{inel} = \sigma_{el} + \sigma_{sd} + \overline{\sigma}_{sd} + \sigma_{dd} + \sigma_{nd} \tag{1}$$

σ_{el} is the elastic cross section, σ_{sd} is the single diffractive cross section when the incoming proton fragments into a number of particles, $\overline{\sigma}_{sd}$ is the single diffractive cross section for the fragmentation of the antiproton (at high energies $\sigma_{sd} = \overline{\sigma}_{sd}$). σ_{dd} is the double diffractive cross section, σ_{nd} is the non-diffractive part of the inelastic cross section.

The elastic, single diffractive and double diffractive processes give rise to low multiplicity events with particles emitted in the very forward and very backward regions in the c.m. system. The non-diffractive cross section is the main part of the inelastic cross section; the non-diffractive processes give rise to high multipliciy events and to particles emitted at all angles. Most of the non-diffractive cross section concerns particles emitted with low transverse momentum (low p_t physics) with properties which change slowly with c.m. energy (*ln s* physics)[22]. A relatively small part of the non-diffractive cross section is due to central collisions among the colliding particles and gives rise to high p_t jets of particles emitted at relatively large angles (*large* p_t physics). The contribution of jet physics increases with c.m. energy.

There is as yet no unique interpretation of the data in terms of a fundamental theory, like QCD; the data are interpreted in terms of a number of phenomenological models, each of which enphasizes some aspects of the theoretical picture [23-24].

In this short review, first the basic formulae of the processes under study, then the experimental methods employed at the highest energy fixed target accelerators and at colliders will be briefly summarized; this is followed by a discussion of total cross section and elastic scattering data. The data are then interpreted in terms of phenomenological models. A conclusion and an outlook follow.

2. Basic formulae

For high energy hadron-hadron scattering, we shall use the standard variables s, the c.m. energy squared, and t, the square of the momentum transferred.

Over a limited t-range, say fot $|t| < 0.15\ (GeV/c)^2$, the nuclear part of the elastic scattering cross section may be expressed as an exponential in t:

$$d\sigma/dt = (d\sigma/dt)_{t=0}\ \exp(bt) \tag{2}$$

The optical theorem relates the forward differential cross section, $(d\sigma/dt)_{t=0}$, with the total cross section σ_{tot},

$$\sigma_{tot}^2 = \frac{16\pi(\hbar c)^2(d\sigma/dt)_{t=0}}{1+\rho^2} \tag{3}$$

where ρ is the ratio of the real-to-imaginary part of the forward nuclear elastic scattering amplitude.

In the Coulomb-Nuclear interference region ($0.001 < |t| < 0.01\ (GeV/c)^2$) the differential elastic cross section (for $\overline{p}p$ scattering) may be written as

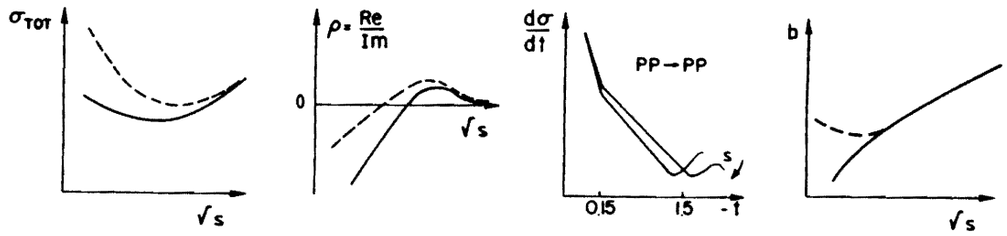

Figure 2 - Illustration of the high-energy behaviour of the total cross section, of the ratio ρ of the real to the imaginary part of the forward elastic scattering amplitude, of the differential elastic scattering cross section shapes and of their slopes b for $|t|<0.1$ $(GeV/c)^2$.

$$\frac{d\sigma}{d|t|} = \underset{\text{Coulomb}}{C^2} + \underset{\text{Nuclear}}{\frac{(1+\rho^2)\sigma_{tot}^2}{16\pi(\hbar c)^2}\, exp(bt)} + \underset{\text{C}-\text{N Interference}}{\frac{\alpha(\rho-\alpha\phi)G^2\sigma_{tot}}{|t|}\, exp(bt/2)} \tag{4}$$

where C is the Coulomb amplitude

$$C = \frac{2\sqrt{\pi}\alpha\hbar c}{|t|} G^2(t)\, \exp(i\alpha\phi) \tag{5}$$

and

$G(t)$ = proton form factor $\simeq (1+|t|/0.71)^{-2}$, t in $(GeV/c)^2$,

ϕ = phase of coulomb amplitude relative to nuclear $\simeq \ln(0.08/|t| - 0.577)$,

α = fine structure constant $\simeq 1/137$.

Relation (3) is valid on the hypothesis that ρ does not depend on t and that spin effects are negligible. It contains three parameters, ρ, b and σ_{tot}, which we shall consider to be the fundamental parameters of high energy elastic scattering and total cross sections. Fig. 2 shows a sketch of the behaviour of these parameters with increasing c.m. energies. A fourth parameter, the opacity $O = 2\sigma_{el}/\sigma_{tot}$, may be obtained as the ratio of the integrated elastic cross section to the total cross section. At high energies, this parameter is slowly increasing with increasing energy.

Other measurable quantities to be considered are the single and double diffractive cross sections σ_{sd} and σ_{dd} [25-27].

For $|t| < 0.001$ $(GeV/c)^2$ Coulomb scattering dominates.

For a discussion of the high energy theorems, the reader is referred to reviews [4] and to more specialized review papers. Here it will only be recalled that the Froissart bound says that the total cross section may rise at most as $\sigma_{tot} \leq (\pi/m_\pi^2)(\ln s/s_0)^2$

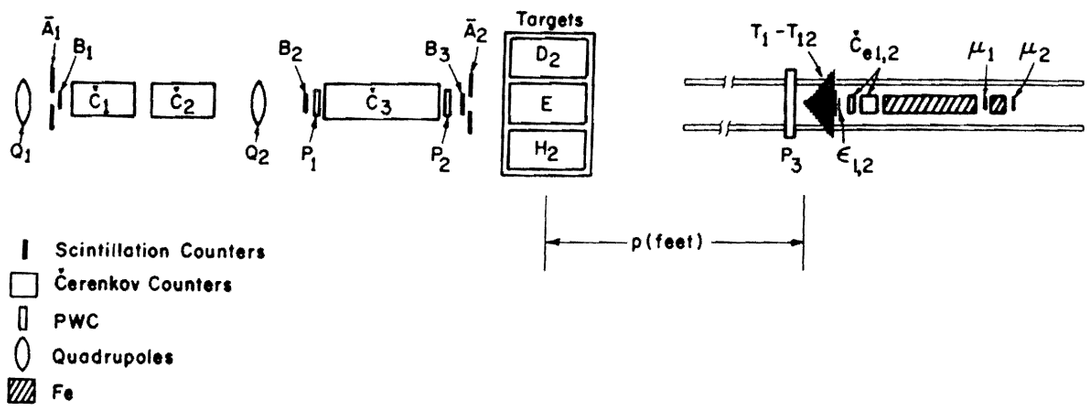

Figure 3 - Layout of the charged particle total cross section measurements performed at Fermilab[14]. The incoming beam is counted as $B=B_{123}\overline{A}_{12}C_i$, where C_i is one or a combination of the three gas Cherenkov counters C_1-C_3. P1-P3 are proportional wire chambers. D_2, H_2 and E are targets, with liquid hydrogen, liquid deuterium and "dummy". T_1-T_{12} are transmission counters. E_1 and E_2 are small counters used for beam tuning and for measurement of the efficiences of the transmission counters. $\hat{C}_e$ is a lead glass Cherenkov counter; μ is a combination of two large scintillation counters.

and that the second Pomeranchuck theorem states that in the limit $s \to \infty$ the total cross sections on the same target particle of particle and antiparticle become equal.

3. Experimental methods

We shall briefly discuss the transmission method, which was used at several fixed target accelerators to measure the total cross sections of hadrons, and the methods of measurements of elastic and total cross sections at pp and $\overline{p}p$ colliders.

3.1 The total cross sections at fixed targed accelerators. The trasmission method

Fig. 3 shows the typical layout used for the precision measurements of the total cross sections of charged hadrons ($\pi^{\pm}$, $K^{\pm}$, $p^{\pm}$) on proton and deuteron targets. The method was employed successfully at the Brookhaven 33 GeV AGS, the Serpukhov 76 GeV protonsynchrotron and at the 400 GeV Fermilab protonsynchrotron. Schematically, the layout consists of i) a system of counters to count the incoming particles, ii) a number of targets where the incoming beam is absorbed, and iii) a series of cylindrical transmission counters, each subtending a different solid angle from the target.

The measurement consists in determining the fraction of transmitted particles with and without the target. This leads to the determination of the partial cross

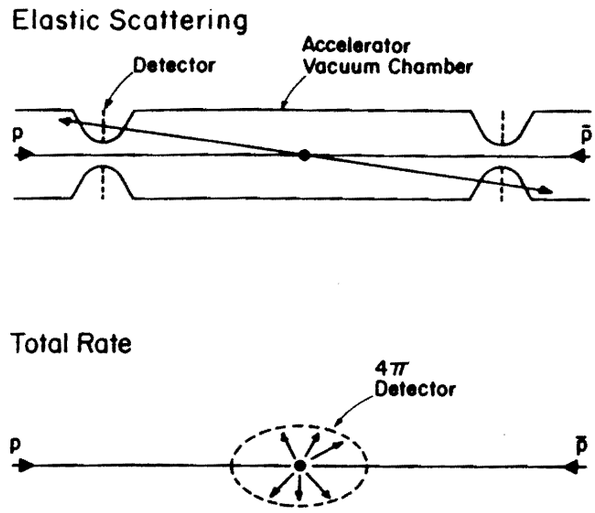

Figure 4 - Schematic of elastic scattering and total cross section measurements methods at hadron colliders.

section σ_i for each of the trasmission counter i. σ_{tot} is then obtained by an extrapolation of the partial cross sections to zero solid angle.

Several improvements in the technique and in data handling were made over the years, which made it possible to measure total cross sections with point-to-point precisions of $\pm 0.1\%$ and with a systematic scale error of about $\pm 0.4\%$.

3.2 Total cross sections and elastic scattering measurements at $\bar{p}p$ colliders

Fig. 4 shows two sketches of the experimental methods used at the $S\bar{p}pS$ and Fermilab $\bar{p}p$ colliders to measure $\bar{p}p$ elastic scattering and total cross sections. Elastic scattering is measured by detectors in "Roman pots", which can be moved to very small distances from the circulating beams; at the same time, the total rate is determined using a "4π" detector.

A more detailed layout of experiment E710 at the Fermilab collider is shown in Fig. 5. It consisted of four "Roman pots" at four locations along the beam axis. The outer "pots" were embedded in the magnetic lattice of the accelerator and were used for elastic scattering at very small angles. Each "pot" contained a drift chamber with four sense wires, two scintillation counters for triggering purposes and a scintillation counter, with several holes and hedges, for calibration of the chamber. Notice that $|t| = 0.001\ (GeV/c)^2$ means $\theta \simeq \sqrt{|t|}/p \simeq 3.5 \times 10^{-5} rad$ at $\sqrt{s} = 1800\ GeV$. This means that the detectors are at few millimeters from the circulating beams in the "pots" at about 100 m from the collision region. Furthermore this requires dedicated runs with very parallel (high β) beams, and performing "scraping" of the beams to reduce beam halos (see Fig. 6).

On either side of the interaction region, there were five sets of ring-shaped scintillation counters, covering the range $4.0 < \eta < 6.5$, where $\eta = -ln\ tan\theta$ is the pseudorapidity. There were also drift chambers (not shown in Fig. 5) for tracking

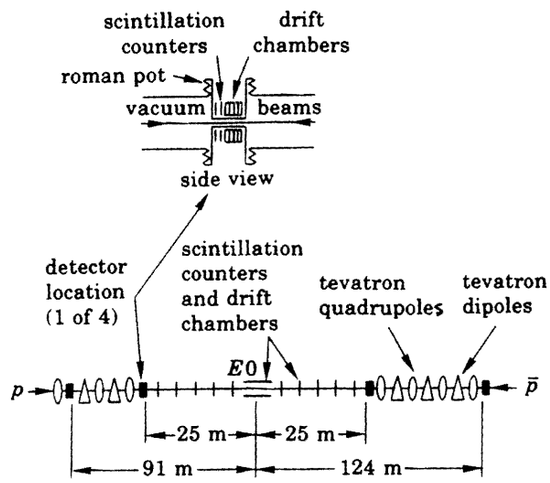

Figure 5 - Schematic layout of the E710 apparatus[18].

in the pseudorapidity range 6.0 to 6.5. The double arm rate, that is the rate in which at least one particle was recorded on either side of the collision region, was almost all due to inelastic $\bar{p}p$ interactions; the ranges of η covered were sufficient to measure properly the inelastic non-diffractive cross section σ_{nd}. The determination of the single diffraction cross section is more difficult. The single arm rate, giving events with counters hits only on one side of the collision region, could yield the single diffractive cross section. The rate was affected by a large background. But in specialized runs with some proton bunches and some antiproton bunches missing it was possible to estimate the background. The single arm rate was thus corrected for background, for losses at small and large angles (by extrapolation using the tracking chambers and counters).

A similar layout was used at the $S\bar{p}pS$ collider[17]; at Fermilab the CDF Collaboration used silicon microstrip detectors in the usual "Roman pots" [20-21].

Different methods have been used for the measurement of the total cross sections at $\bar{p}p$ colliders. We shall briefly consider five methods.

i) The most direct method involves the measurement of the total collision rate, N_{tot}, and of the integrated luminosity L. The total cross section is

$$\sigma_{tot} = \frac{N_{tot}}{L} = \frac{N_{el} + N_{inel}}{L} \tag{6}$$

N_{el} e N_{inel} are the corrected number of elastic and inelastic events and L is the integrated luminosity during that period of data taking, $L = \int_0^t \mathcal{L}\, dt$.
In practice the different processes are detected with different efficiencies ϵ_i; the detected cross section, σ_{det}, is given by (letting $\sigma_{el} = f\ \sigma_{tot}$, $\sigma_{sd} = \bar{\sigma}_{sd}$):

$$\sigma_{det} = \sigma_{el}\epsilon_{el} + 2\sigma_{sd}\epsilon_{sd} + \sigma_{dd}\epsilon_{dd} + \sigma_{nd}\epsilon_{nd} = N_{det}/L\epsilon \tag{7}$$

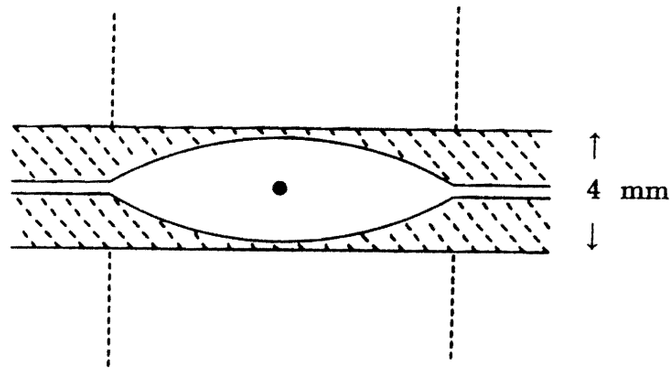

Figure 6 - Sketch of the beam spot and of the E710 detectors located at the Fermilab collider intersection region E0[18].

Thus the total cross section is

$$\sigma_{tot} = [\sigma_{det} + 2(\epsilon_{nd} - \epsilon_{sd})\sigma_{sd} + (\epsilon_{nd} - \epsilon_{dd})\epsilon_{dd}]/[\epsilon_{nd}(1-f) + \epsilon_{el}f] \tag{8}$$

The precision of the method is limited by the systematic error on the luminosity ($\pm 15\%$) and by the knowledge of the single diffractive cross section. The luminosity was determined from the measurement of the transverse dimensions of the beams. Because $\sigma_{tot} \sim 1/L$, one cannot have a percentage error smaller than $\pm 15\%$. Moreover, with a "4π" detector the efficiencies for elastic scattering and for single diffraction are small: $\epsilon_{el} \sim 0.07$, $\epsilon_{sd} \sim 0.1$ ($\epsilon_{dd} \sim 0.5$). Thus separate measurements of elastic and single diffraction scattering are needed.

ii) The second method is based on the measurement of elastic scattering in the region $0.01 \leq |t| < 0.1$ $(GeV/c)^2$ and on the use of the optical theorem. From Eqs. (2,3) and the definition of luminosity, $L = N/\sigma$, one has:

$$\sigma_{tot}^2 = \frac{1}{L}\frac{16\pi(\hbar c)^2}{1+\rho^2}\left(\frac{dN}{dt}\right)_{el,nucl,t=0} \tag{9}$$

In this case $\sigma_{tot} \approx 1\sqrt{L}$ and thus the percentage scale error is about 7%.

iii) The luminosity independent method. Taking the ratio of (9) to (8) one has

$$\sigma_{tot} = \frac{16\pi(\hbar c)^2}{1+\rho^2}\frac{(dN/dt)_{el,nucl,t=0}}{N_{el}+N_{inel}} \tag{10}$$

N_{el} may be obtained by integrating the elastic angular distribution.

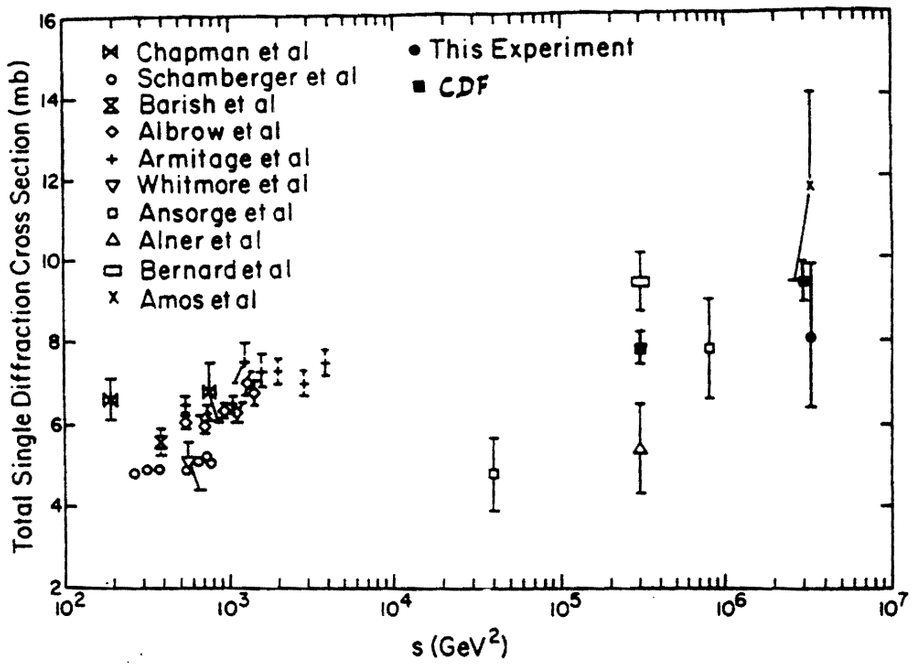

Figure 7 - A compilation of measurements of the total single diffractive cross section in pp and $\bar{p}p$ collisions versus s. "This experiment" is E710 [25].

iv) From the simultaneous measurements of elastic scattering in $0.001 < |t| < 0.1\ (GeV/c)^2$ and of the inelastic processes one has a more interconnected situation, described by Eqs. (1-5), (9-10). One can thus determine together ρ, σ_{tot} and L.

v) From a simultaneous measurement of the calculable Coulomb scattering in $10^{-4} < |t| < 10^{-3}(GeV/c)^2$ one could determine the integrated luminosity L. In practice this method was not used until now.

With method (iv), the total cross sections were measured to precisions of about 5-10%. The inelastic single diffractive cross section is not known to better than 15%, see Fig. 7.

4. Total cross sections

Fig. 8 shows, as function of laboratory momentum, three compilations of the measured total and integrated elastic cross sections for π^+p, π^-p and K^+p scattering, respectively.

The π^+p cross section is for a pure $I = 3/2$, πN state. At low energies, one observes the dominant (3/2, 3/2) resonance and smaller peaks and structures; then σ_{tot} decreases smoothly, reaches a minimum and increases slowly with energy. The π^-p state is a mixture of I=1/2 and I=3/2, πN states. At low energies the total cross section has more peaks than for π^+p. At higher energies, $\sigma_{tot}(\pi^-p)$ is slightly larger than $\sigma_{tot}(\pi^+p)$; the difference decreases as the energy increases.

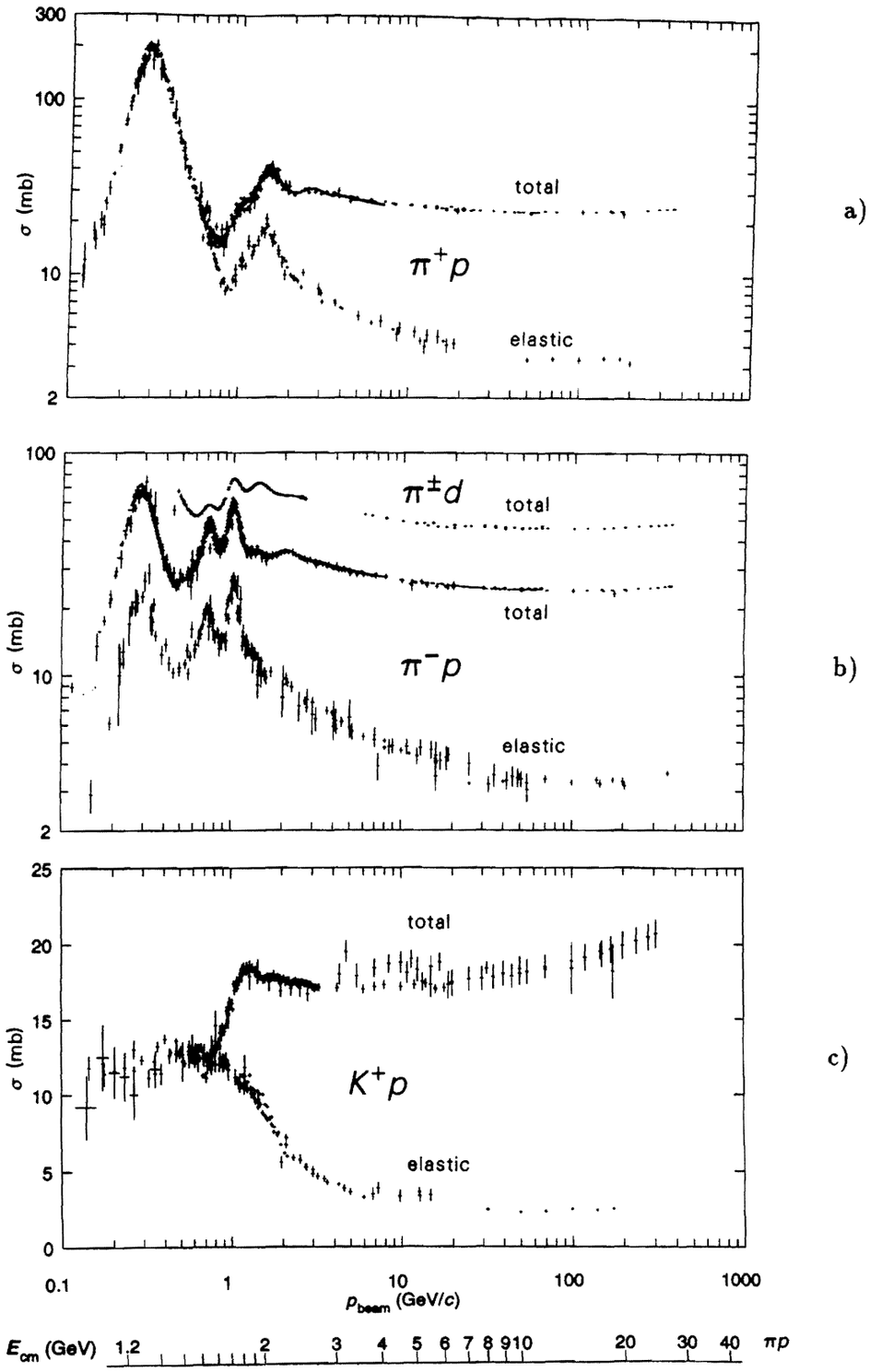

Figure 8 - Compilations of data of the total and of the integrated elastic cross sections versus lab momentum for (a) π^+p, (b) π^-p and π^-d (c) K^+p scattering [3].

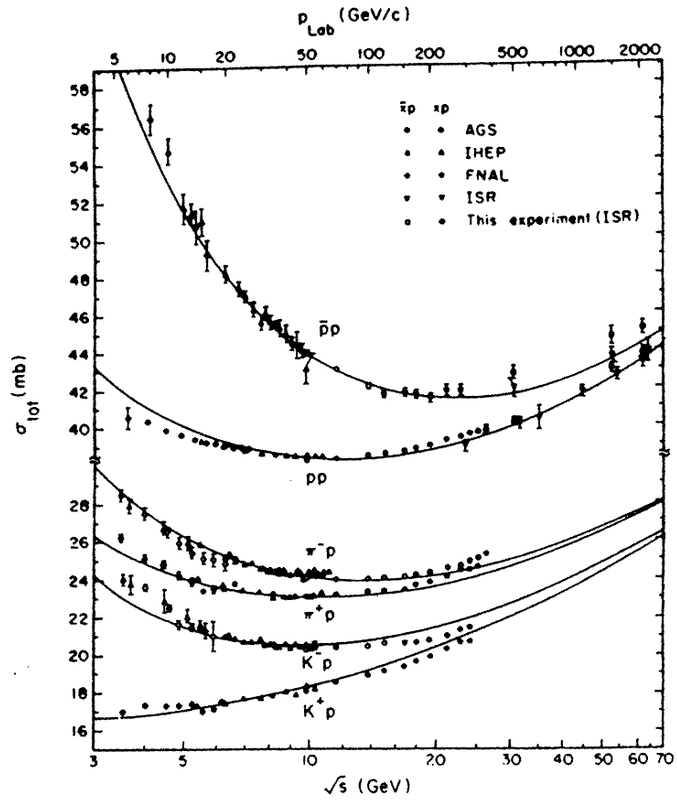

Figure 9 - Total cross sections for high-energy hadron-hadron scattering. The curves are computed according to Lipkin's parametrization[14].

The K^+p cross section does not have prominent structures at low energies, but only a step followed by some oscillations[1]. The cross section starts to rise already at relatively low energies: its rise was already evident and established at Serpukhov energies[6].

The behaviour of the $\bar{p}p$, pp, π^-p, π^+p, K^-p and K^+p cross sections versus energy for c.m. energies between 3 and 70 GeV is summarized in Fig. 9. The figure shows that, as the energy increases, the first five cross sections decrease, reach a minimum and then increase. The K^+p cross section increases in this entire range. All the differences $[\sigma_{tot}(\bar{x}p) - \sigma_{tot}(xp)]$ decrease with increasing energy; Fig. 10 illustrates the behaviour of the total cross section difference for $\bar{p}p$, pp.

Fig. 11 illustrates the behaviour of $\sigma_{tot}(\bar{p}p)$ for c.m. energies of 10-1800 GeV ($\sigma_{tot}(pp)$ is shown as a dashed line). Fig. 12 shows a compilation of $\bar{p}p$ and pp total cross sections, including cosmic ray measurements. The data are well described by the empirical fit of Amaldi et al. [9], repeated recently by Augier et al. [17] (solid line of Fig. 12; the dashed lines delimit the region of uncertainty, while the dotted line corresponds to $\gamma = 1$, see below). They fitted the high energy data for σ_{tot} and ρ for pp and $\bar{p}p$ scattering using once subtracted dispersion relations for odd and even

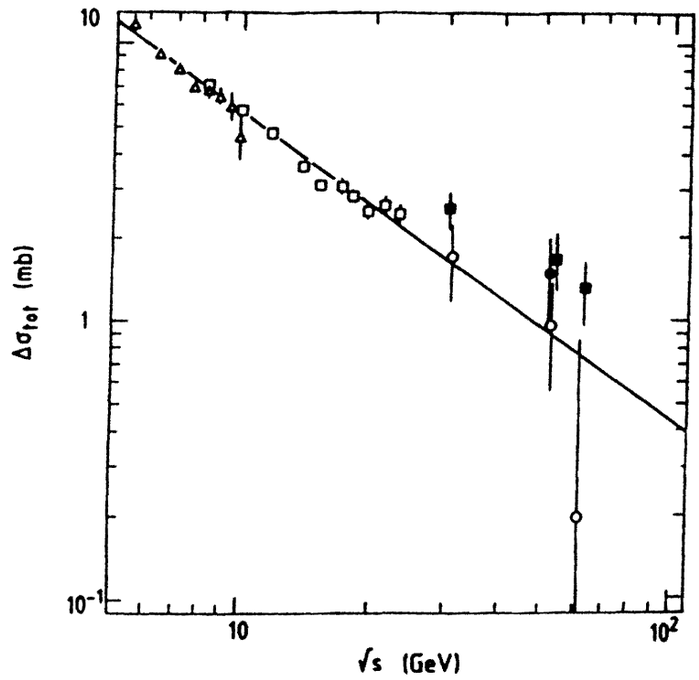

Figure 10 - The difference between $\bar{p}p$ and pp total cross sections versus $\sqrt{s}$ [4].

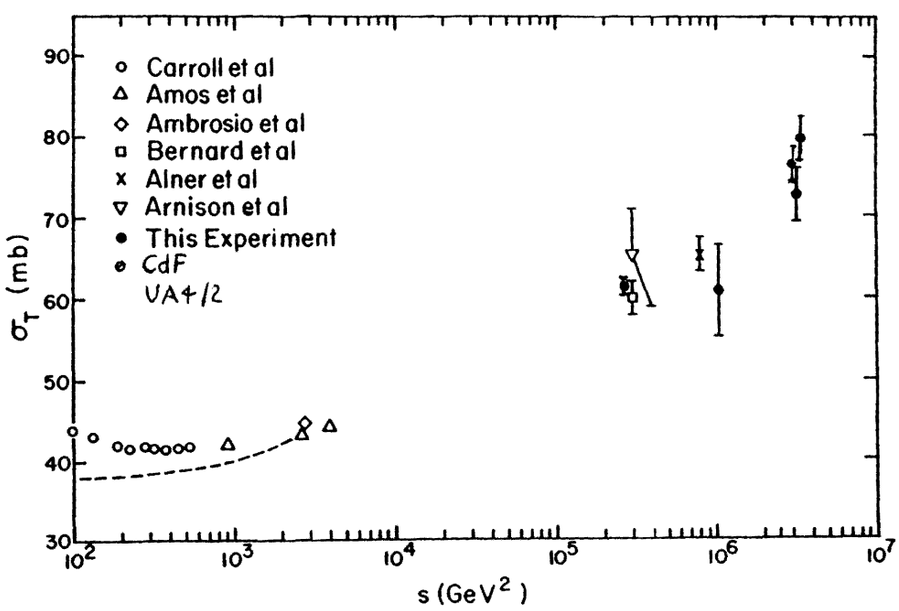

Figure 11 - Compilation of high energy $\bar{p}p$ total cross sections. The dashed line indicates a fit through the pp total cross sections[14].

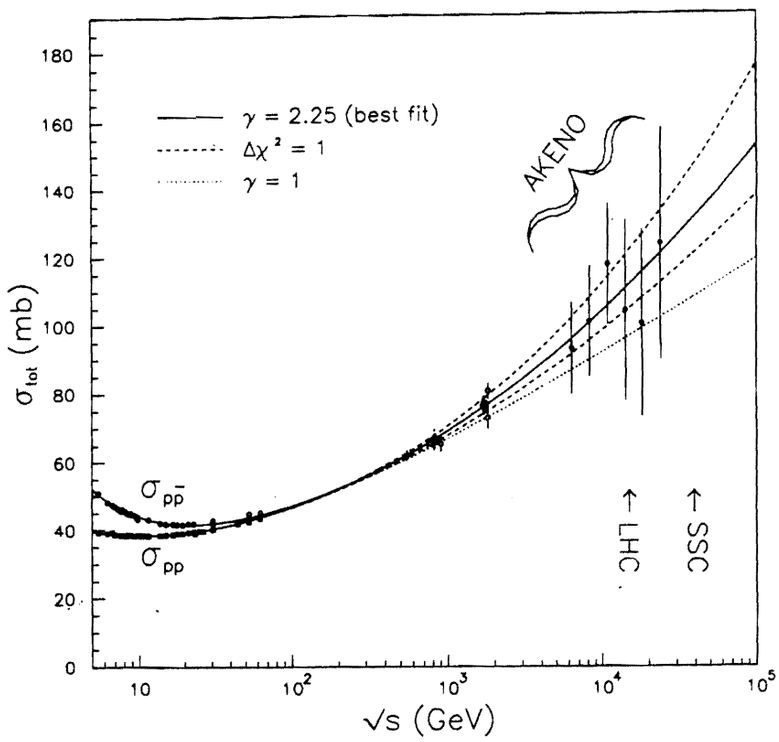

Figure 12 - Compilation of $\bar{p}p$ and pp total cross sections including cosmic ray measurements. The solid line is a fit of the σ_{tot} and ρ data with dispersion relations [17,9]; the region of uncertainty is delimited by dashed lines.

under crossing forward amplitudes, assuming that the odd part becomes negligible at very high energies. In order to evaluate the integral over the total cross sections, they assumed the following parametration

$$\sigma_{\pm}(E) = A_1 E^{-N_1} \mp A_2 E^{-N_2} + \sigma_{\infty} \tag{11}$$

where

$$\sigma_{\infty} = C_0 + C_2 \; [ln \; (s/s_0)]^{\gamma} \quad , \quad s_0 = 1 \; GeV^2 \tag{12}$$

The terms $A_1 E^{-N_1}$ and $A_2 E^{-N_2}$ are Regge type terms which describe the behaviour at relatively low energies and the difference between $\sigma_{tot}(\bar{p}p)$ and $\sigma_{tot}(pp)$. E is the energy of the incoming particle in the lab system.

In eqs. (11, 12) there are eight parameters which may be determined by the fit to the data; the fit has a $\chi^2/DoF = 78.5/95$. In particular one has $C_0 = 30^{+3}_{-4}$, $C_2 = 0.10^{+0.15}_{-0.06}$ and $\gamma = 2.25^{+0.35}_{-0.31}$. Notice the approximate $ln^2 \; s$ behaviour of the

very high energy σ_{tot}. The fit predicts $\sigma_{tot} = (111 \pm 8)mb$ and $\rho = 0.133 \pm 0.018$ for pp scattering at the future LHC collider ($\sqrt{s} = 16\ TeV$).

Successful fits to σ_{tot}, ρ and b have also been done by M. Block et al [28] in the context of a QCD inspired model.

5. Elastic scattering

Results of the measurements of the elastic scattering differential cross section for pp and $\bar{p}p$ at the CERN ISR [29,30] ($\sqrt{s} = 53\ GeV$), at the CERN $S\bar{p}pS$ ($\sqrt{s} = 541\ GeV$) and at Fermilab [19] ($\sqrt{s} = 1.0$ and $1.8\ TeV$) for different ranges of t are shown in Figures 13 and 14. Globally the data are in reasonable agreement within the experimental errors. The data show the Coulomb-nuclear interference pattern in $\bar{p}p$ scattering at small values of t ($\sqrt{s} = 541\ GeV$) (Fig. 13a), a double exponential slope in pp collisions at $\sqrt{s} = 53.4\ GeV$ in the $0.05 < |t| < 0.4\ (GeV/c)^2$ range[29], a single exponential pattern in $\bar{p}p$ scattering at $\sqrt{s} = 1.8\ TeV$ in the range $0.01 < |t| < 0.5(GeV/c)^2$ (Fig. 14b), and the dip-bump structure in pp at $\sqrt{s} = 53\ GeV$ at larger t-values; the structure seems to get filled up in $\bar{p}p$ collisions at the same energy and is considerably reduced at $S\bar{p}pS$ energies (Fig. 14a). The shrinking of the diffraction pattern is also clearly seen from Figures 13-14.

Detailed analyses of the $\bar{p}p$ elastic scattering data at the highest avaible energies yielded values of the elastic scattering slope b, at the average values of $|t| \sim 0.1$ (and $\sim 0.2(GeV/c)^2$) and of the ρ parameter; the integration of the elastic differential cross sections yielded σ_{el} and then the ratios σ_{el}/σ_{tot} (see Figures 15-16). There is reasonable agreement among the data from different experiments, within their relatively large uncertainties.

The slope parameter b for $\bar{p}p$ keeps increasing from ISR energies to the highest Fermilab energies, at a rate which is probably larger than $ln\ s$. The elastic $\bar{p}p$ cross section continues to rise, at a rate close to $ln^2\ s$ or larger. Therefore the ratio σ_{el}/σ_{tot} increases with energy, reaching the value of about 0.24 at $\sqrt{s} = 1.8\ TeV$. This value is still far below the black disk value of 0.5. However the Fourier transformation of the t-distribution yields a form factor, which at $r = 0$ has reached the value of 0.5; this means that the center of the proton has become opaque, almost black.

From Fig. 14b it is apparent the interest in new measurements of $\bar{p}p$ elastic scattering at $\sqrt{s} = 1.8\ TeV$ in the $0.5 < |t| < 1\ (GeV/c)^2$ region to establish if the dip-bump structure effectively exists, and to check at lower values of t and at lower energies if the diffraction pattern has really gone from a

$$\frac{d\sigma}{dt} = Ae^{bt+ct^2} \tag{13}$$

shape with c positive to a shape with $c = 0$, as suggested by the E710 data at 1.8 TeV. Some models predict that at higher energies the c value should become negative; thus the diffraction pattern would approach the classical diffraction pattern from a disk of radius R and opacity a, described by a Bessel function of order 1, J_1:

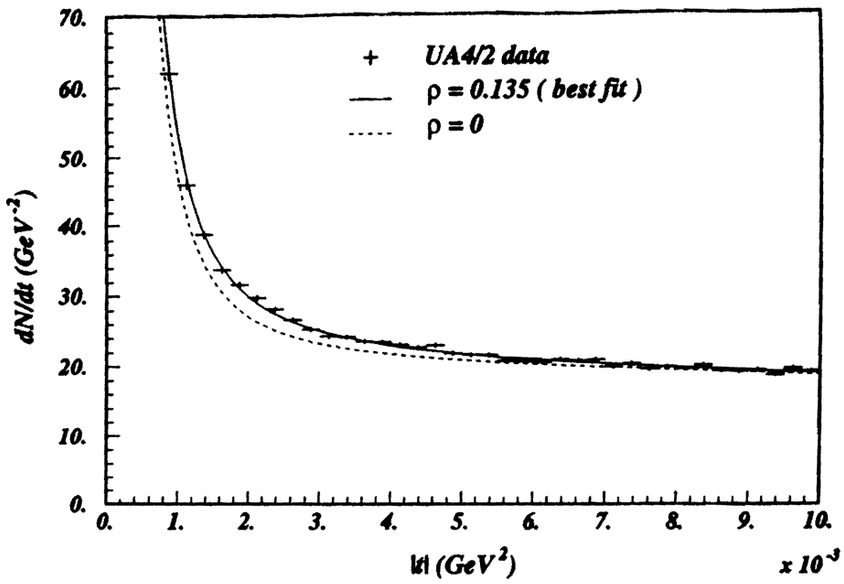

a)

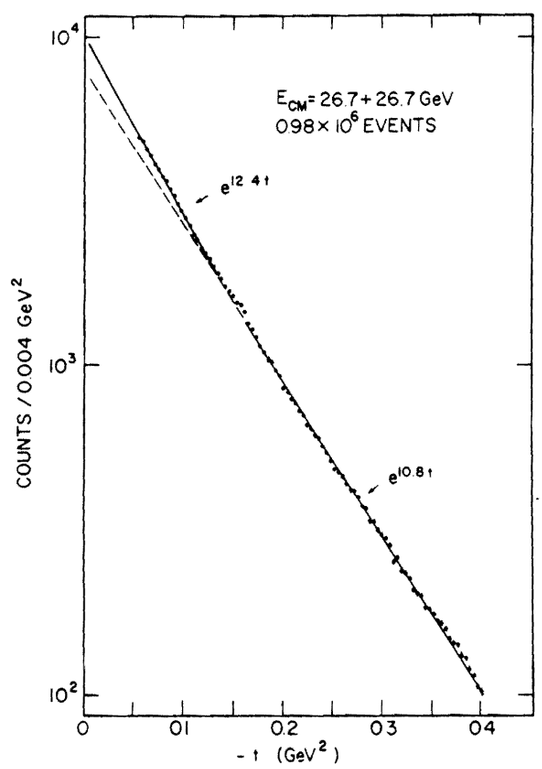

b)

Figure 13 - Differential elastic scattering cross sections (a) for $\bar{p}p$ in the Coulomb-nuclear interference region at $\sqrt{s}$=541 GeV at the CERN collider [17], and (b) for pp at the CERN ISR, $\sqrt{s}$=53.4 GeV [18].

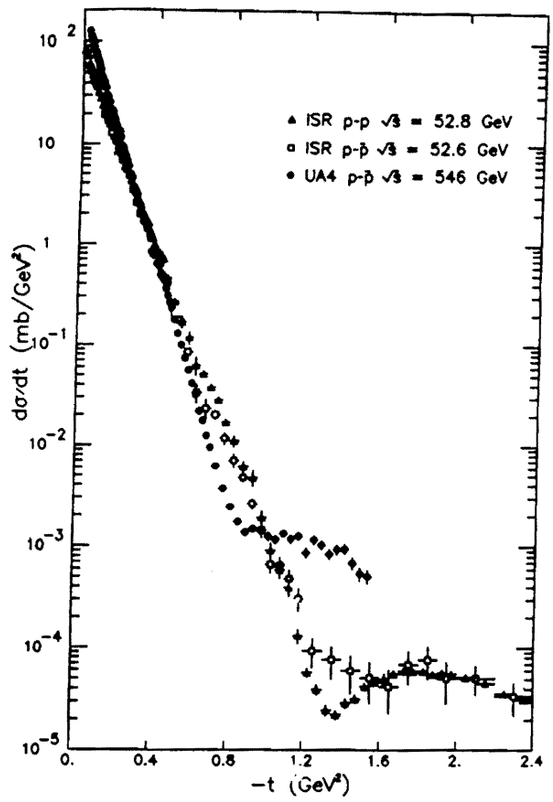

a)

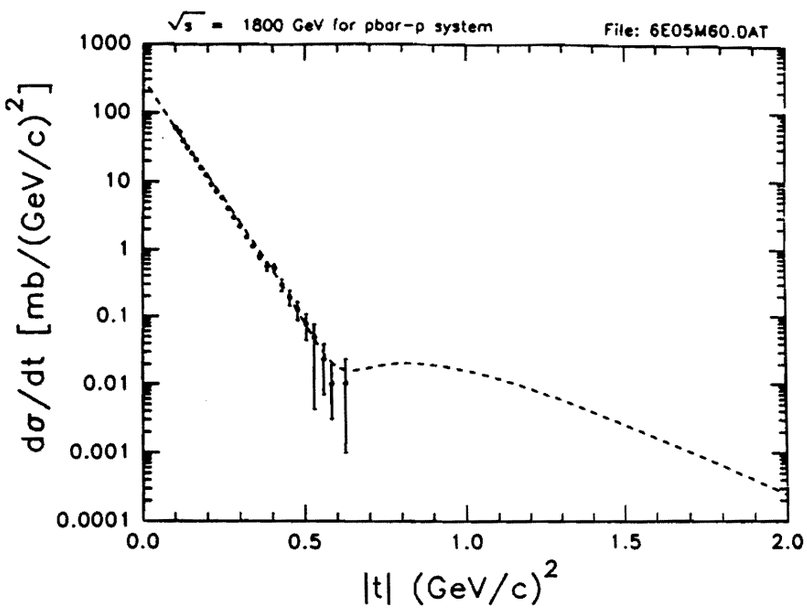

b)

Figure 14 - Differential elastic scattering cross section (a) for pp and $\bar{p}p$ at $\sqrt{s}$=53 GeV and for $\bar{p}p$ at $\sqrt{s}$=546 GeV [24-31], and (b) for $\bar{p}p$ at $\sqrt{s}$=1800 GeV at Fermilab [19], together with a fit by Block et al. [28].

$$\frac{d\sigma}{dt} \simeq (1-a)\ \pi R^4 \left[\frac{J_1(R\sqrt{|t|})}{R\sqrt{|t|}}\right]^2 \tag{14}$$

New values of ρ, the ratio of the real to the imaginary part of the $\bar{p}p$ elastic scattering amplitude, were obtained from elastic scattering data in the Coulomb-Nuclear interference region. The new values of ρ, see Fig. 17, follow the dispersion relation calculations.

In most elastic scattering analyses the polarization effects are neglected, since such effects are thought to decrease as the energy increases; besides they are small in the forward direction. In fact sizable and measurable spin and asymmetry effects have been observed at high p_t, where the cross section for pp elastic scattering with spins parallel is about four times larger than the cross section for spins antiparallel at $p_t \sim 2-3\ GeV/c$ [24,36]. Fig. 18 shows the analyzing power A as a function of momentum transfer p_t^2 for spin-polarized proton-proton elastic scattering at 24 GeV/c: polarization effects are quite evident at relatively large values of p_t^2.

Polarization effects are also present in pion production at large Feynman$-x$, with π^+ and π^- showing opposite behaviours in their production with respect to the spin direction of the target proton. Spin effects need to be investigated more systematically, both experimentally and theoretically.

6. Conclusions and outlook

From the latest experimental results at the highest $\bar{p}p$ collider energies and from cosmic ray data one may conclude that (i) the total cross section σ_{tot} and the nuclear slope parameter b continue to rise, (ii) the increasing ratio σ_{el}/σ_{tot} indicates that the nucleon becomes blacker as energy increases, (iii) the nuclear curvature parameter of Eq. 13 is compatible with zero at $\sqrt{s} = 1.8\ TeV$; this result compared with the positive values measured at lower energies may signal the transition to a really asymptotic region, where c should be negative and the nucleon would behave more like a black sharp disc. (iv) The measurements of the single diffraction scattering (SDD) cross section indicate that it has a smaller energy dependence. But it must be warned that there is no unique experimental definition of SDD. (v) There is no more an anomalous ρ-value, see Fig. 17..

Since the early 1970 Serpukhov experiments, one knows that the total cross sections rise with energy, but there is as yet no unique explanation for this phenomenon. From a theoretical point of view, although we have a theory of the strong interaction, its implications for total cross section and elastic scattering are not clear.

It must be re-stated that elastic scattering is the shadow of particle production; therefore a real knowledge of elastic scattering requires the knowledge of particle production. At relatively low energies, say $\sqrt{s} \leq 0.1\ TeV$, particle production in hadron-hadron collisions exhibits Feynman scaling and KNO scaling; jet production is a rare phenomenon and tranverse momenta are limited[22]. At higher energies the production of jets becomes dominant and affects minimum bias events; high p_t-events are also high multiplicity events. The $< p_t >$-value increases with energy,

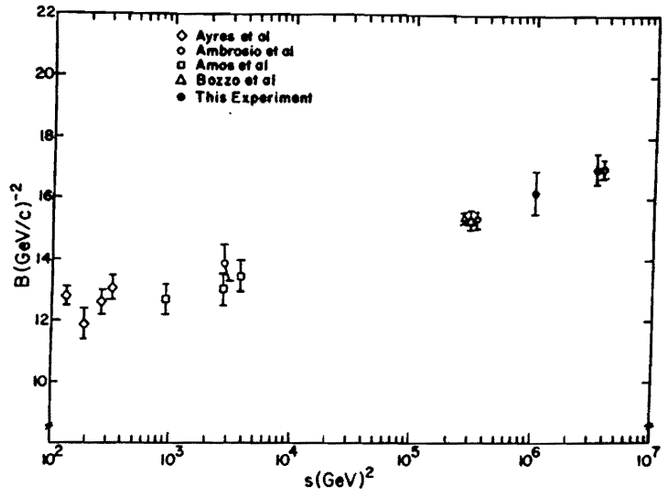

Figure 15 - Slope B of the $\bar{p}p$ elastic scattering distributions at $<|t|>\simeq 0.1\ (GeV/c)^2$ [14].

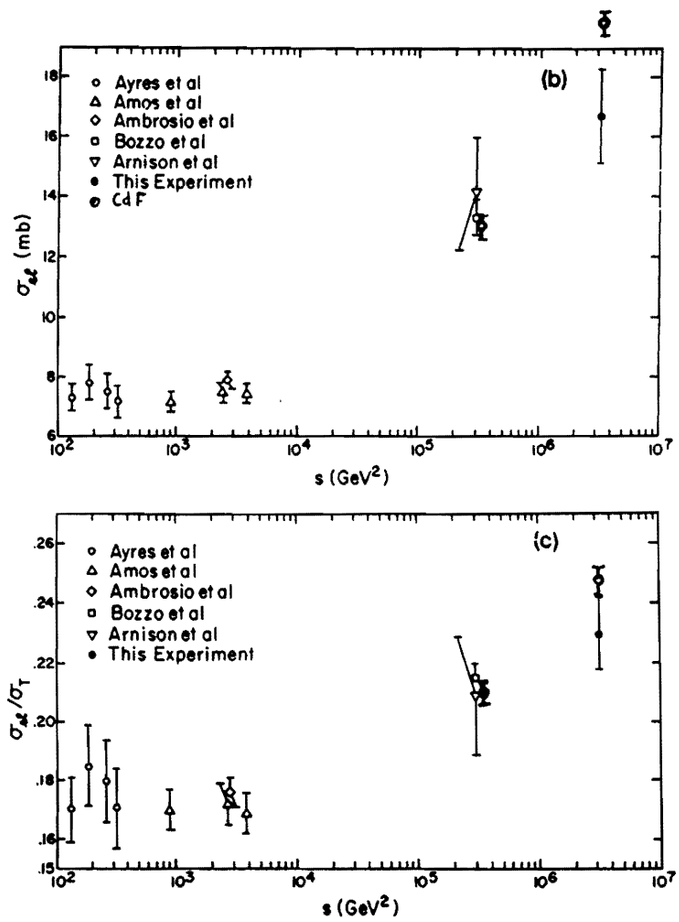

Figure 16 - (a) Integrated $\bar{p}p$ elastic cross sections plotted versus s. (b) Ratio of the elastic to total cross section for $\bar{p}p$ versus s [14].

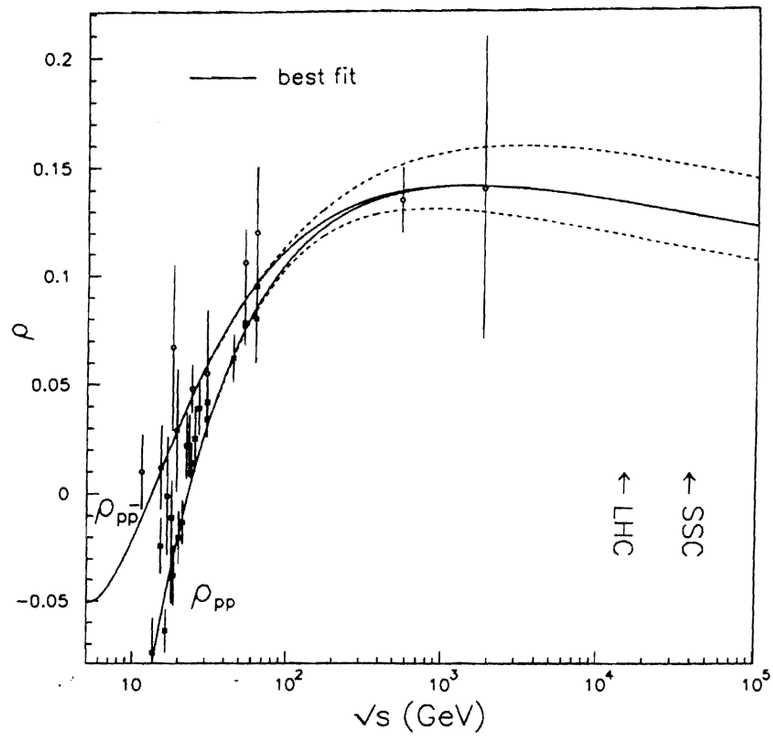

Figure 17 - Ratios ρ the real to imaginary part of the forward $\bar{p}p$ elastic scattering amplitude plotted versus $\sqrt{s}$. The solid line is the result of the UA4/2 fit [17], the dashed lines delimit its uncertainties.

Feynman scaling is violated in the central region and the KNO distribution starts to exhibit a high multiplicity tail[22].

The interpretation of elastic scattering and total cross section data was mostly done in terms of Pomeron exchange. The new single diffraction dissociation data allow to extend this analysis also to SDD.

Although the Pomeron was introduced many years ago, there still are differences in its exact definition and in its detailed substructure. Many models have been proposed to explain the rising hadron-hadron cross sections in terms of the behaviour of the Pomeron.

Donnachie and Landshoff[29] proposed a "soft Pomeron" amplitude, in which the Pomeron is described as a ladder of Reggeons, yielding an effective Regge trajectory of

$$\alpha(t) = 1.08 + 0.2\ t \tag{15}$$

The rising cross sections arise from $\alpha(t = 0) = 1.08$. For energies higher than $\sqrt{s} \simeq 20\ GeV$ they may be represented by the formula

$$\sigma_{tot} \simeq 22\ s^{0.08} \tag{16}$$

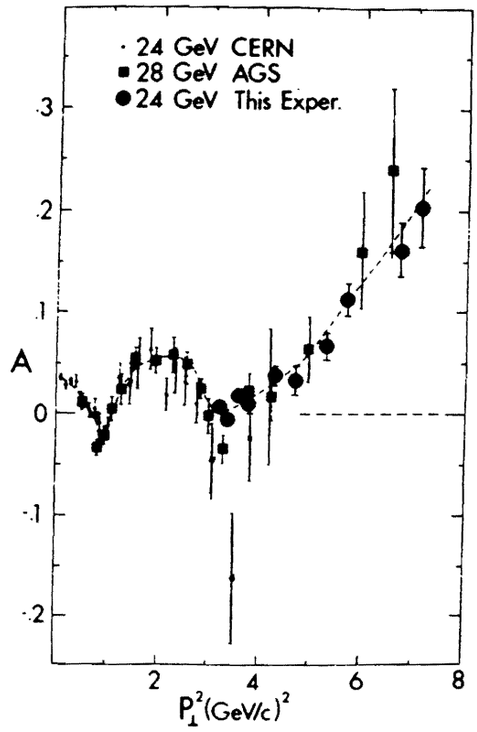

Figure 18 - The analyzing power A as a function of momentum transfer $P_\perp^2$ for spin polarized proton-proton elastic scattering at 24 GeV/c. The error bars include both the statistical and systematic errors. The dashed curve is a han-drawn curve to guide the eye[36].

(s in GeV^2). This simple model reproduces well the experimental data.

In a second approach the Pomeron is viewed as a gluon ladder. In perturbative QCD this Pomeron receives its major contribution for high p_t gluon exchanges (it may be called a "hard Pomeron").

Bjorken suggested that the generic Pomeron may manifest itself in both soft and hard modes, each contributing in a different kinematical domain. Also these models reproduce the data [32,33].

In QCD inspired models the rise of σ_{tot} is associated with the increasing probability of semi-hard gluon interactions. The experimental data are well described in a mixed model containing soft $q-q$ and semi hard $q-g$ and $g-g$ interactions[28].

The above models of the Pomeron yield a power rise of the total cross section, $\sigma_{tot} \sim s^{\alpha_0}$. Thus the Pomeron amplitude violates the s-channel unitarity, at energies slightly larger than those of the Tevatron collider. This problem is eliminated with proper eikonalization: the amplitudes obtained from the models discussed above are considered to be the lowest order input to the eikonal expansion [34,35]. These models are also capable of reproducing the high energy main features of single diffraction dissociation, in particular the moderate dependence of σ_{sd} on s.

As already stated in most analyses the polarization effects are neglected and it came as a surprise that polarization effects are still measurable at high energies[36]. More experimental and theoretical work seems to be needed in this field.

The future experimental outlook remains for the moment centered on the Fermilab collider, where new measurements of elastic and total cross sections will be made in the near future [37]. The future after the year 2000 awaits the approval construction and operation of the LHC collider at CERN.

7. Acknowledgements

I would like to thank all the members of the E710 Collaboration for their cooperation and encouragement. I thank members of the CDF and UA4 Collaborations for discussions and for providing data. I thank several theoretical colleagues for explanations and discussions. I thank Mrs. B. Simoni Bonacorsi for her enthusiastic help with the manuscrip and Dr. P. F. Spada for correcting the manuscript.

8. References

1. R.J. Abrams et al., Phys. Rev. D1 (1970) 1917. See this paper for further references on low energy total cross sections.
2. G. Giacomelli , Progress in Nuclear Phys. 12 (1970) 77.
3. Particle Data Group, Review of Particle Properties, Phys. Rev. D45 (1992) N.11.
4. G. Giacomelli, Phys. Rep. 23C (1976) 124.
5. J.V. Allaby et al., Phys. Lett. 30B (1969) 500; Yad. Fisika 12 (1970) 538; CERN-NP-70-4 (1970); S. P. Denisov et al., Phys. Lett. 36B (1971) 528.
6. S.P. Denisov et al., Phys. Lett. B36 (1971) 415, 528; Yad. Fisika 14 (1971) 998; Nucl. Phys. B65 (1973) 1.
7. G. B. Yodh et al., Phys. Rev. Lett. 28 (1972) 1005.
   Akeno Coll., M. Honda et al., Phys. Rev. Lett. 70 (1993) 525.
8. U. Amaldi et al., Phys. Lett. 62B (1976) 460; Phys. Lett. 66B (1977) 390; Nucl. Phys. B145 (1978) 367.
9. S.R. Amendolia et al., Phys. Lett. 44B (1973) 119; Nuovo Cimento 17A (1973) 735.
10. G. Carboni et al., Phys. Lett. B108 (1982) 145; D. Favart et al., Phys. Rev. Lett. 47 (1981); Bozzo et al., Phys. Lett. 147B(1984) 392.
11. G. Giacomelli and M. Jacob, Phys. Rep. 55 (1979) 1, and 1980 updating, 25 years of CERN, North Holland Publ. Co. (1981).
12. N.A. Amos et al., Nucl. Phys. B262 (1985) 689; Phys. Rev. Lett. 61 (1988) 525.
13. A. Breakstone et al., Nucl. Phys. B248 (1984) 253.
14. A. S. Carroll et al., Phys. Rev. Lett. 33 (1974) 928, 932; Phys. Lett. B61 (1976) 303; Phys. Rev. Lett. 80B (1979) 423; see this paper for further references.
15. D.S. Ayres et al., Phys. Rev. D15 (1977) 3107; V. Bartenev et al., Phys. Rev. Lett. 29 (1972) 1755; G. Barbiellini et al., Phys. Lett. 39B (1972) 663; see this papers for further references.
16. UA4 Coll., D. Bernard et al., Phys. Lett. B 171 (1986) 142; B155 (1985) 197.
17. UA4/2 Coll., C. Augier et al., CERN/PPE 93-115 (1993) and Phys. Lett B, to be published; CERN-PPE/93-121(1993), and Phys. Lett. B, to be published.
18. E710 Coll. N. Amos et al., Phys. Rev. Lett. 61 (1988) 525; Phys. Rev. Lett. 63 (1989) 2784; Phys. Lett. B234 (1990) 158; Phys. Lett. B247 (1990) 127; Phys. Rev. Lett. 68 (1992) 2433.
19. E710 Coll., N.A. Amos et al., Nuovo Cimento A106 (1993) 123.

20. CDF Coll., F. Abe et al., FERMILAB-Pub-93/232-E, Phys. ReV D
21. CDF Coll., F. Abe et al., FERMILAB -Pub–93/234-E, Phys. Rev. D
22. G. Giacomelli, Int. Jour. Mod. Phys. A5 (1990) 223.
23. F. Halzen (Blois V: Summary talk) MAD/PH/772 (1993) and Proceedings of the Vth Blois Workshop on Elastic and Diffractive Scattering (1993).
24. M.G. Albrow (Blois V: Experimental Summary) FERMILAB-Conf-93/266 and Proceedings of the Vth Blois Workshop on Elastic and Diffractive Scattering (1993).
25. E710 Coll., N. Amos et al., Phys. Lett. B243 (1990) 158; Phys. Lett. B301 (1993) 313.
26. CDF Coll., F. Abe et al., FERMILAB-Pub-93/233-E and Phys. Rev. D, to be published.
27. K. Goulianos, Phys. Rep. 101 (1983) 169; see this paper for further references; E. Gotsman et al. (Diffractive dissociation and eikonalization in high energy pp and $\bar{p}p$ collisions) FERMILAB-Pub-93/292-T (1993).
S. Barshay et al., (Elastic scattering and single diffraction dissociation in $p(\bar{p})-p$ collisions up to 1000 TeV) PITHA 92/8 (1992).
28. M.M. Block et al., Phys. Rev. D41 (1990) 978; D47 (1993) 101; (High Energy behaviour of σ_{tot}, ρ and B - Asymptotic amplitude analysis and a QCD inspired analysis) NUHEP Rep. 304 (1993) and Proceedings of the Vth Blois Workshop on Elastic and Diffractive Scattering (1993).
29. A. Donnachie and P.V. Landshoff, Nucl. Phys. B231 (1984) 189; Phys. Lett. B296 (1992) 227.
30. L.N. Lipatov, Sov. Phys. JETP 63 (1986) 904.
31. J. D. Bjorken, Nucl. Phys. (Proc. Suppl.) B25 (1992) 253.
32. E. Gotsman et al., Zeit. Phys. C57 (1993) 667.
33. J. R. Cudell and B. Margolis, Phys. Lett. B297 (1992) 398.
34. T.T. Chou and C.N. Yang, Phys. Rev. 170 (1968) 1591; Phys. Lett. B128 (1983) 457; L. Durant and R. Lipes, Phys. Rev. Lett. 20 (1968) 637.
35. E. Gotsman et al. (Diffractive dissociation and eikonalization in high energy pp and $\bar{p}p$ collisions) FERMILAB-Pub-93/292-T (1993).
36. A.D. Krisch, Proceedings of the Vth Blois Workshop on Elastic and Diffractive Scattering (1993); D.G. Crabb et al., Phys. Rev. Lett. 65 (1990) 3241.
37. J. Orear et al., Fermilab Experiment E811 and CDF Collaboration.

NAME	[illegible]	M.S.
WOLBERS	6807	120

RETURN TO FERMILAB LIBRARY